

Article

# The Role of Interfacial Effects in the Impedance of Nanostructured Solid Polymer Electrolytes

Martino Airoidi , Ullrich Steiner <sup>\*</sup>  and Ilja Gunkel 

Adolphe Merkle Institute, University of Fribourg, Chemin des Verdiers 4, 1700 Fribourg, Switzerland; martino.airoidi@polymat.eu (M.A.)

<sup>\*</sup> Correspondence: ullrich.steiner@unifr.ch

**Abstract:** The role of interfacial effects on an ion-conducting poly(styrene-*b*-ethylene oxide) (PS-*b*-PEO or SEO) diblock copolymer doped with lithium bis(trifluoromethanesulfonyl) imide (LiTFSI) was investigated by electrochemical impedance spectroscopy (EIS). Coating the surface of commonly used stainless steel electrodes with a specific random copolymer brush increases the measured ionic conductivity by more than an order of magnitude compared to the uncoated electrodes. The increase in ionic conductivity is related to the interfacial structure of the block copolymer domain morphology on the electrode surface. We show that the impedance associated with the electrode–electrolyte interface can be detected using nonmetallic electrodes, allowing us to distinguish the ionic conductivity behaviors of the bulk electrolyte and the interfacial layers for both as-prepared and annealed samples.

**Keywords:** solid polymer electrolyte; impedance; interfacial effects



**Citation:** Airoidi, M.; Steiner, U.; Gunkel, I. The Role of Interfacial Effects in the Impedance of Nanostructured Solid Polymer Electrolytes. *Batteries* **2024**, *10*, 401. <https://doi.org/10.3390/batteries10110401>

Academic Editor: Claudio Gerbaldi

Received: 16 October 2024

Revised: 29 October 2024

Accepted: 4 November 2024

Published: 12 November 2024



**Copyright:** © 2024 by the authors. Licensee MDPI, Basel, Switzerland. This article is an open access article distributed under the terms and conditions of the Creative Commons Attribution (CC BY) license (<https://creativecommons.org/licenses/by/4.0/>).

## 1. Introduction

The global transition to next-generation energy sources has been accelerated by recent technological advances in portable devices, renewable energy storage, new industries such as electric vehicles, and the dwindling fossil fuel reserves [1,2]. Lithium-ion batteries (LIBs) continue to dominate the battery market. Still, the growing demand over the past decade, coupled with the anticipated future growth [3], has driven research to improve LIB performance, particularly in increasing energy and power densities [4]. Next-generation electrode materials are therefore designed to increase battery capacity and operating voltage [5,6]. High-voltage cathode materials such as LiCoMnO<sub>4</sub> and LiNiPO<sub>4</sub> [7–9] allow battery operation at 5 Volts, while advances in anode materials [10–12], particularly promising metallic lithium, aim to increase the energy density [13].

However, challenges are associated with integrating such advanced electrodes with liquid electrolytes (LEs), particularly with organic-based LEs, due to their limited electrochemical stability window [14]. The high reactivity of the metallic lithium anodes in contact with the liquid electrolyte causes dendrite formation [15] during battery cycling [16,17]. This is dangerous due to the risk of short circuits and thermal runaway processes, which can ignite the carbonaceous electrolyte and accumulate dead lithium aggregates and insoluble by-products. These materials precipitate at the electrode–electrolyte interface, forming a complex, mosaic-like structure: the solid electrolyte interphase (SEI) [18–20]. Thickening of the SEI over cycling life leads to progressive battery capacity fading [21,22].

Replacing the commonly used liquid electrolytes with solid-state electrolytes (SSEs), prominent classes of which were reviewed by Manthiram et al. [23], allows increases in safety, mechanical properties, and the electrochemical stability window [24]. Among SSEs, solid polymer electrolytes (SPEs) stand out for their exceptional mechanical properties. They can withstand both extrinsic mechanical stresses during processing and intrinsic stresses, such as those caused by dendrite growth and thermal expansion of the electrodes during cycling.

Polyethylene oxide (PEO)-based systems remain the dominant choice for SPEs [25–27]. They offer competitive transference numbers, electrochemical stability, and high ionic conductivity. Their effective ionic transport stems from lithium-ion coordination by the ether-oxygens along the polymer backbone and the fast segmental motion at the relevant temperatures, characterized by PEO's relatively low glass transition temperature [28]. However, like other homopolymers, PEO faces a trade-off between its mechanical properties and ionic transport [29]. Fast segmental motion allows efficient ion transport but renders the polymer soft, while slow chain motion hinders ion transport but stiffens polymers.

To overcome this trade-off, multicomponent polymers such as block copolymers (BCPs) can be used instead of homopolymers. BCPs, such as PS-*b*-PEO (SEO), consist of a soft, ion-conducting polymer, such as PEO, linked to a stiff, non-conducting block, like polystyrene (PS). The unique property of BCPs to self-assemble into various morphologies, including spheres, cylinders, lamellae, and gyroids [30], allows the design of nanostructured ion conductors reinforced by a rigid phase [31]. This allows independent control and tuning of stiffness and conductivity by the BCP composition. Moreover, these two fundamental properties depend on the specific morphology of the ion conductor [32].

The effect of morphology on the ionic conductivity in block copolymer (BCP) electrolytes is typically described by the equation  $\sigma_{\text{BCP}} = f\phi_c\sigma_c$ , where  $\sigma_c$  is the intrinsic conductivity of the conducting phase,  $\phi_c$  is the volume of the conducting phase, and  $f$  is a structural parameter [33,34]. Ideally,  $\sigma_c$  should match the electrolyte conductivity of the corresponding homopolymer ( $\sigma_{\text{HP}}$ ), and  $f$  is an ideal morphology factor (1 for gyroids, 2/3 for lamellae, 1/3 for cylinders, and 0 for spheres) accounting for the pathway's degree of freedom of ion transport in the different BCP morphologies. However, the conductivity in the ion-conducting phase of BCP electrolytes is often lower than that of the corresponding homopolymer ( $\sigma_c \neq \sigma_{\text{HP}}$ ). This discrepancy is due to the interface between the ion conductor and the non-conductor in BCPs, which results in a region within the conductor that cannot coordinate lithium ions effectively and has limited segmental mobility [35]. The resulting additional conductivity reduction is observed in thick [36] and thin films [37] and is referred to as the dead zone or inactive volume.

It is possible to precisely control BCP structures in thin films to achieve defect-free morphologies with well-aligned structures by directing the self-assembly of, for example, PS-*b*-PEO lamellae [37]. Together with the ability to precisely control and image defects in the nanostructured ion conductor [38], which cause unwanted conductivity drops, this establishes a precise relationship between structure and conductivity performance. However, controlling defects in thick BCP films, which are more common in practical battery designs, is challenging. This often results in the formation of defects such as ion transport dead ends and grain boundaries, leading to multi-grain structures.

Interestingly, multi-grain SPEs with small grain sizes increase the ionic conductivity compared to larger, more refined grains [39]. Moreover, increasing the molar mass of a BCP electrolyte increases the overall conductivity, plateauing at around 1 mS/cm for PS-*b*-PEO lamellae [40]. However, understanding ion transport in these multi-grain structures is difficult due to multiple interrelated factors, including the inactive conductive volume, grain size, defect types, density, and their relationship to the BCP molar mass and annealing protocols. The intricate interplay between these factors makes it difficult to distinguish between intrinsic features on the ion transport, such as the interface between the non-conducting and conducting phases causing tethered chain confinement, and extrinsic factors such as defects and grain boundaries [41–43].

This complexity is compounded by preferential wetting of the BCP structure at the electrode interface [44], which has recently been shown to reduce ionic conductivity significantly. However, ionic transport in BCP electrolytes at the electrode interface is not clearly understood. Overall, achieving precise control of the structure in BCP electrolytes is challenging, and the intricate interplay of structural parameters and a limited understanding of the underlying structure–property relationships make optimizing conductivity in thick BCP electrolytes a complex task.

Two recent studies address the interfacial conductivity of a BCP containing an ionic liquid block, forming a single ion conducting microphase. Measuring the DC conductivity of thick BCP layers sandwiched between silicon wafers reveals a 20-fold difference between transverse and in-plane conductivities, attributed to the formation of lamellar layers covering the silicon electrodes [45]. A follow-up study of similar BCPs attributed the anisotropic conductivities to variations of in-plane rather than transverse conductivities [46]. Interestingly, a comparison of rough stainless steel versus smooth silicon substrates showed similar transverse conductivities despite substrate-induced BCP layering in the latter.

This work aims to extend the knowledge of polymer electrolyte thin films to thick films, ultimately optimizing their ionic conductivity. The investigated thickness of the electrolyte film, less than 100  $\mu\text{m}$ , is significantly larger than both nanometer-scale BCP domain spacing and brush layer. The approach is based on controlling the structure of a lamellar PS-*b*-PEO BCP electrolyte at the interface with the electrode by chemically tuned surface coatings to avoid unwanted conductivity drops. The ionic conductivity response of the electrolyte on such chemically engineered electrodes was measured by electrochemical impedance spectroscopy and assessed by analyzing various derived electrochemical quantities. Additionally, the effect of annealing on the ionic conductivity was studied to elucidate the relationship between the electrolyte's grain structure and ionic transport.

## 2. Materials and Methods

### 2.1. Materials

Lithium bis(trifluoromethanesulfonyl)imide, anisole (anhydrous, 99.7%), and tetrahydrofuran (anhydrous  $\geq 99.9\%$ , inhibitor-free) were purchased from Sigma Aldrich (Buchs, Switzerland). Poly(styrene-*block*-ethylene oxide) and poly(styrene-*random*-2-vinyl pyridine) were purchased from Polymer Source (Dorval, QC, Canada). Silicon wafers were purchased from Si-Ma Silicon Materials (Kaufering, Germany). Stainless steel disks were purchased from MTI (Richmond, CA, USA).

### 2.2. Sample Fabrication

All materials and chemicals were dried in a vacuum oven at 80  $^{\circ}\text{C}$  for 24 h before transferring to an argon-filled glovebox ( $<0.01$  ppm  $\text{O}_2$  and  $\text{H}_2\text{O}$ ). They were used without further purification. The poly(styrene-*block*-ethylene oxide) copolymer and LiTFSI were dissolved in anhydrous anisole in a molar salt concentration

$$r = \frac{[\text{Li}^+]}{[\text{EO}]}, \quad (1)$$

targeting a value of  $r = 0.08$ , corresponding to optimization by [40,47]. The solution was drop-cast into PTFE washers, which were placed on the respective electrodes: stainless steel or silicon wafers, pristine or covered by a random poly(styrene-*random*-2-vinyl pyridine) copolymer brush.

The casting and manipulation of the samples were performed inside an argon-filled glovebox ( $<0.01$  ppm  $\text{O}_2$  and  $\text{H}_2\text{O}$ ). The samples were assembled by sandwiching the SPE between identically prepared electrodes into sealed Swagelok cells inside the glovebox, followed by their removal from the glovebox for measurements.

P(S-*r*-2VP) end group modification: Conversion of P(S-*r*-2VP)-RAFT agent to P(S-*r*-2VP)-SH: 0.8 g of P(S-*r*-2VP) was dissolved in 7 mL anhydrous THF in a two-neck flask in a nitrogen atmosphere. A small amount of  $\text{Na}_2\text{S}_2\text{O}_4$  was added after polymer dissolution and 1 mL hexylamine was added to the mixture and stirred at room temperature overnight. The solution was filtered, and the yellowish solution was dropwise added to a cold hexane bath for polymer precipitation. The solid residue was then dried in a vacuum oven at 50  $^{\circ}\text{C}$  overnight.

Brush-covered stainless steel electrode preparation: Substrate disks were cleaned with acetone before sputtering an approx. 5 nm thick gold layer onto one side. The gold-coated substrate was immersed in a 0.015 mM solution of the thiol-terminated statistical copolymer,

P(S-*r*-2VP)-SH, in deionized water overnight, allowing the homogeneous coverage of the stainless steel substrate. The brush-covered substrate was then rinsed with fresh THF to remove the excess unbranched polymer and placed in a vacuum oven at 80 °C for 12 h before import into the glovebox, resulting in a solvent-free nanometer-thick brush layer on the metallic substrate.

**Brush-covered silicon electrode preparation:** The silicon wafer was cleaned with acetone and air plasma-treated for 10 min to introduce hydroxyl functional groups on the surface. Brushing the substrate was achieved by spin coating a 0.015 mM statistical copolymer brush, P(S-*r*-2VP), solution in THF on the polished silicon wafer and annealed at 150 °C for 1 h to end graft the polymer to the SiO<sub>2</sub> surface. The procedure is fully described elsewhere [44]; note that the copolymer has a hydroxyl terminal group, and therefore, no further chemical modifications were required. The substrate was then rinsed with THF to remove any ungrafted polymer and placed in a vacuum oven at 80 °C for 12 h before transfer into the glove box.

**Annealing protocol:** Annealing was performed in a Binder vacuum oven under N<sub>2</sub>. The dwell time was 1 hour with a ramp rate of about 2 °C min<sup>-1</sup> followed by cooling to room temperature.

### 2.3. Electrochemical Impedance Spectroscopy (EIS)

EIS data were acquired using an SP-300 BioLogic Potentiostat (Seysinnet-Pariset, France), in single sine scanning mode, covering a frequency range between 5 MHz and 0.1 Hz, measuring 10 frequencies per decade. The amplitude was set to 100 mV, and an average of 3 measurements per frequency was taken with a resolution of 333 μV per measurement. The temperature of the Swagelok cell was controlled in a Binder oven with ≈1 h dwell time for temperature equilibration, covering a temperature range from room temperature to 95 °C in 15 °C intervals. The impedance data obtained were fitted using the Z-fit function of the EC-Lab V10.44 software employing the adequate equivalent circuit shown in Figure 1.

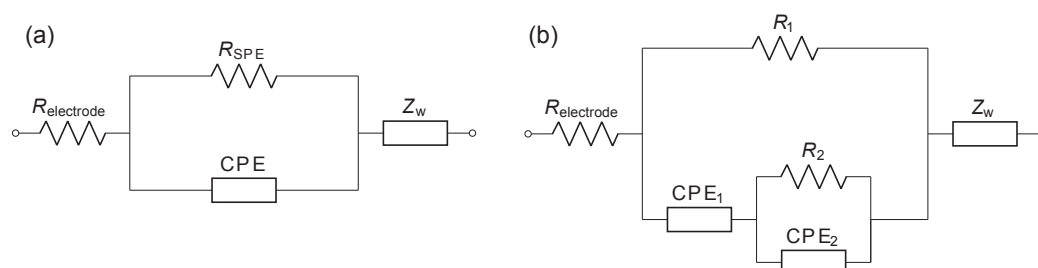


**Figure 1.** Equivalent circuits used to fit the Nyquist plots showing single or multiple Randles circuits for the case of stainless steel (a) and silica (b) substrates.

The ionic conductivity values were calculated using

$$\sigma = \frac{1}{R} \frac{L}{S_A}, \quad (2)$$

where  $R$  is the resistance derived from the equivalent circuit fitting,  $L$  is the thickness of the electrolyte layer, and  $S_A$  is the surface area of the electrode–electrolyte interface. For clarity, the reported ionic conductivity lines are the averages derived from three separate samples. The sample geometry was maintained using PTFE washers of two different sizes: one with a length of 0.8 mm and a radius of 4.3 mm and the other with a length of 0.4 mm and a radius of 3.2 mm.

### 2.4. Atomic Force Microscopy (AFM)

Atomic force microscopy images were taken by a Park NX10 instrument (Suwon 16229, Republic of Korea). All measurements were performed in an acoustic enclosure

(JPK Instruments AG, now: Bruker, Billerica, MA, USA) equipped with an antivibration table (e-Stable mini, Kurashiki Kako, Tokyo, Japan). The acquired images were leveled by mean-plane subtraction and second-order polynomial baseline removal. The look-up table was adjusted to increase the contrast of image features. Profile fitting was performed using the Gwyddion software, v. 2.66.

### 3. Results and Discussion

The impedance behavior of a high-molar-mass poly(styrene-*b*-ethylene oxide) (SEO; block molar masses:  $M_w^{PS} = 90$  kg/mol and  $M_w^{PEO} = 94$  kg/mol) BCP solid polymer electrolyte (SPE) was studied by electrochemical impedance spectroscopy (EIS). The polymer electrolyte was doped with lithium bis(trifluoromethanesulfonyl) imide (LiTFSI) at an 8% molar ratio between lithium cations and ethylene oxide monomer units.

Two types of electrodes were employed to assess the impact of interfacial effects on the impedance of the SPE: stainless steel and silicon wafers. Additionally, both electrodes were tested in their pristine state and after coating with a P(*S-r*-2VP) statistical copolymer brush ( $M_w^{PS-P2VP} = 6$  kg/mol, with a molar styrene:2-vinylpyridine ratio of 66:33), altering their surface chemistry and SPE wetting behavior. Stainless steel, a frequently employed blocking electrode in EIS analysis, was selected following established literature references [48–50]. Atomic force microscopy of the steel substrate showed micrometer-scale roughness stemming from its manufacturing process (Figure S5). Alternatively, highly polished single-crystalline silicon wafers with sub-micrometer-scale surface roughness were employed as electrode substitutes to aim impedance analysis at the electrode–electrolyte interface. An SPE layer was cast onto one electrode and was contacted by a second identical electrode in a Swagelok cell, applying pressure.

Figure 2 shows Nyquist plots of LiTFSI-doped PS-*b*-PEO SPE, with Figure 2a displaying an SEO layer sandwiched between two pristine stainless steel substrates and Figure 2b showing the SPE sandwiched between two stainless steel electrodes coated with a statistical poly(styrene-*r*-2-vinylpyridine) (P(*S-r*-2VP)) copolymer brush. The response of impedance analysis observed in both sample sets suggests a relaxation process with a single time constant. The term time constant is associated with a relaxation process of the solid electrolyte, which is depicted by the single semicircle in the Nyquist plot and the Gaussian bell curve in the Bode plot. In the equivalent circuit, this process is modeled by a single Randles element. Therefore, the universal equivalent circuit depicted in Figure 2a,b was used to derive ionic conductivities. Control experiments comparing the conductivities of PEO homopolymer sandwiched between pristine and brush-covered stainless steel substrates have been published in [44] and are shown in Figure S2. The Nyquist and Bode plots of these samples are shown in Figure S6.

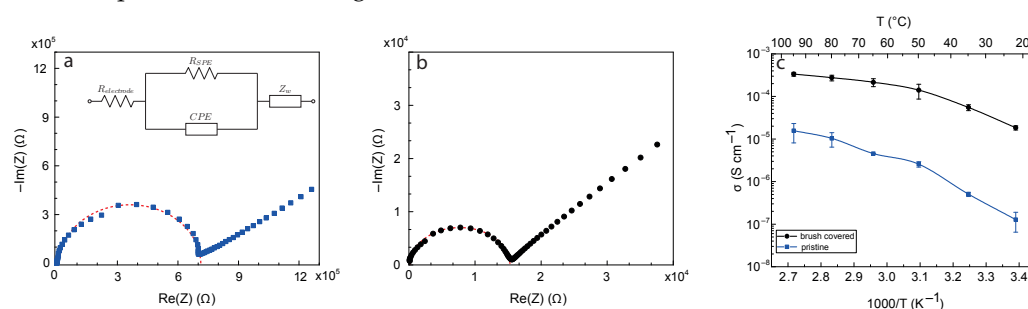


**Figure 2.** Nyquist plot of a PS-*b*-PEO SPE layer sandwiched between two pristine stainless steel electrodes (a) and those coated with statistical P(*S-r*-2VP) copolymer brushes (b). The red semicircles stem from single equivalent Randles circuits, which were used to fit the data (shown in the inset), yielding the ionic conductivity vs. temperature (c).

Significantly different values of the temperature-dependent ionic conductivity of the SPE between the two sample sets were observed, as shown in Figure 2c. Notably, this comparison reveals strongly enhanced ionic conductivities resulting from the brush-coated

electrode, with an increase of more than an order of magnitude compared to the pristine stainless steel electrode. Recent findings demonstrate that coating electrodes with polymer brushes increases the ionic conductivity in gyroid-forming BCP electrolytes after annealing. Brushes favoring the ion-conducting phase in the BCP electrolyte were used to avoid electrode wetting by the non-conducting phase [44].

For the lamellar SEO BCP electrolytes considered here, preventing a layered BCP arrangement at the electrode requires a surface that remains neutral to both PS and PEO, thus avoiding preferential wetting by either block. In BCP thin films, simultaneous wetting of the different blocks of amphiphilic BCPs can be achieved by coating a substrate with “neutral” random copolymer brushes that interpolate between the interfacial energies of the two blocks with the substrate [51]. The morphological arrangement of lamellar BCPs on preferential surfaces and neutral polymer brushes is schematically shown in Figure 3. Starting from the as-cast morphology (left), the BCP arrangement is affected by the chemical nature of the surface. Preferential surfaces (Figure 3a) induce wetting by one of the blocks, leading to lamellar stacking upon annealing. Conversely, neutral surfaces, such as those created by a polymer brush, typically result in the edge-on arrangement shown in Figure 3b.

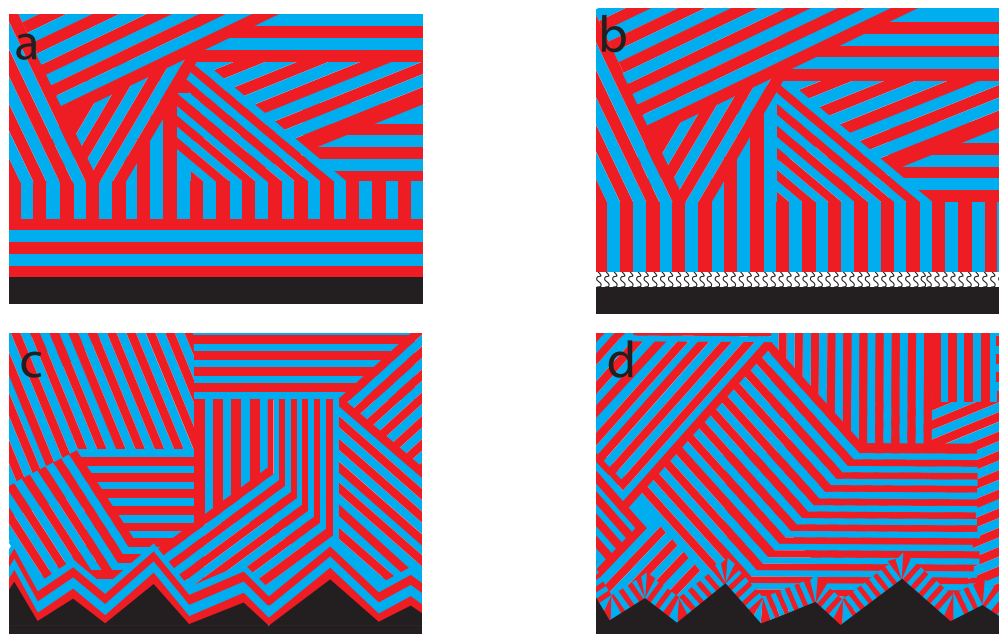


**Figure 3.** Schematic BCP arrangement on preferential and neutral surfaces. (a) BCP layers reorganize into a substrate-parallel lamellar stack adjacent to the pristine silicon wafer substrate while exhibiting an isotropic orientation away from the substrate. (b) Rendering the substrate neutral by a polymer brush results in an edge-on alignment of the BCP lamellae close to the substrate. The two mixed morphologies impact near-surface impedances and ion access to the substrate. Equivalent BCP surface reconstruction on preferential (c) and neutral (d) rougher steel substrates has a less well-defined response of impedance analysis than the smooth silicon surfaces in (a,b). The brush in (d) is omitted for clarity.

Atomic force (AFM) phase images of ca. 140 nm thick SEO layers on pristine and brush-functionalized silicon wafer, Figure S2, demonstrate the effect of the PS-*r*-P2VP brush on the orientation of the SEO BCP morphology, transforming a layered microphase morphology on the pristine surface into one, where the lamellae stand edge-on on the substrate [52]. Water contact angles on substrates are often used as a qualitative measure for the surface polarities of various materials. Table S1 lists the contact angles of the substrates and the electrolyte used in this study. The evolution of surface polarities towards more hydrophobic surfaces while the substrates are coated with the brush is observed. This

result enables comparing the ionic conductivity of SEO layers with differently aligned microphase morphologies.

The surface properties of stainless steel affect the orientation of interfacial SPE BCP domains and, consequently, the diffusion of lithium ions through the BCP domains. In addition, the metallic nature of stainless steel plays an important role in EIS measurements, as charges accumulate at the electrode–SPE interface, inducing polarization (Figure S1). The polarization increases the permittivity of the interfacial layer, thus shielding the input voltage and impeding the observation of relaxation processes away from the interfaces in the bulk of the SPE [53]. To overcome this limitation, a non-metallic substrate was employed, a monocrystalline silicon wafer covered with a thin native SiO<sub>2</sub> layer. This change in the electrode material provided clearer insight into the response of impedance analysis in both the interfacial and bulk SPE regions (Figure 4).

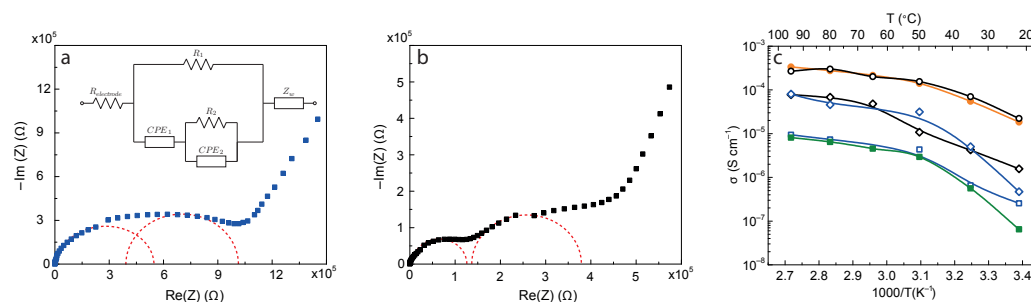


**Figure 4.** Nyquist plots of a PS-*b*-PEO SPE layer sandwiched between two pristine silicon wafer electrodes (a) and between two silicon wafers coated with statistical P(S-*r*-2VP) copolymer brushes (b). The two semi-circles (dashed lines) result from two Randles circuits shown in the inset. This equivalent circuit was used for data fitting to obtain the ionic conductivity values vs. temperature, which are shown together with the temperature-dependent ionic conductivities from Figure 2 (green and orange symbols for pristine and brush-covered surfaces). The blue symbols denote the two time constants and the corresponding conductivities of the pristine silicon wafers, while the black symbols represent the brush-covered silicon wafers (c).

Figure 4a,b shows Nyquist plots of the SPE sandwiched between pristine and random copolymer brush-covered silicon wafers, respectively. The equivalent circuit used to fit the Nyquist plot is expanded to account for its two-semicircle nature (inset in Figure 4a). To achieve this, a second Randles element is incorporated into the previously used fitting circuit, with the additional element representing the second time constant observed in this dataset. Moreover, the additional circuit element is incorporated into the existing Randles element, expressing the interfacial impedance of the polymer electrolyte. Figure 4c shows the derived ionic conductivity values and the temperature-dependent conductivities of one of the two time constants of the pristine and brush-covered silicon wafers match very closely with those of the stainless steel substrates, respectively. The conductivity values derived from the second Randles element lie between those of the two steel substrates. These two curves are comparable in magnitude. The contribution of the silicon wafer to the measurements of Figure 4 is negligible, as can be seen from impedance, which is three orders of magnitude smaller (Figure S4).

In the Bode representation, the impedance gain and phase of the impedance are separately plotted, providing more detailed information on the frequency dependence of the impedance.

Figure 5 shows Bode plots of SPE layers sandwiched between stainless steel (a,b) and silicon (c,d) substrates, pristine (a,c) and copolymer brush-covered (b,d). The orange, green, and red vertical lines mark the peaks in the phase signal of the four measurements.

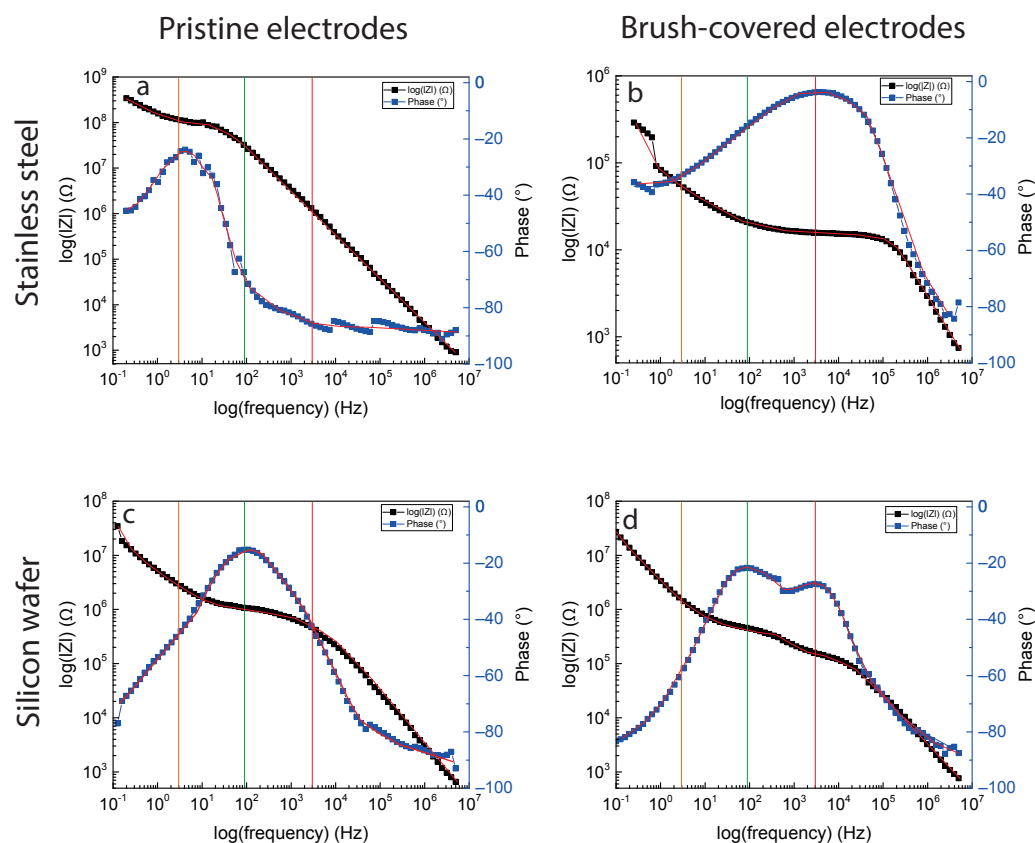


**Figure 5.** Bode plot of PS-*b*-PEO solid polymer electrolyte sandwiched between pristine (a) and statistical P(*S-r*-2VP) copolymer brush-coated (b) stainless steel electrodes. (c,d) show measurements for SPE layers sandwiched between pristine and brush-coated silicon wafers, respectively. The vertical orange, green, and red lines highlight the peaks in the phase signals in (a–d). The fitting profiles are plotted in red.

Each stainless steel experiment exhibits a single plateau in the impedance magnitude and a phase peak, indicating a single time constant in the equivalent circuit of Figure 2. Covering the electrodes with copolymer brushes results in a frequency shift of the phase peak from the Hz (orange) to the kHz (red) regime. When switching to a silicon substrate, the Bode plots show two distinct phase peaks with independent time scales, conforming with the two semi-circles identified in the Nyquist plots. The homogeneity in the phase and impedance gain responses of the polymer electrolyte in the function of the substrate interface design is demonstrated by superimposing the steel and silicon electrode Bode plots. The overlapping of the low- and high-frequency responses of the brushed and pristine electrodes, highlighted by the orange and red lines, respectively, express the uniformity in the SPE response with respect to the substrate design. Additionally, the secondary phase peak that persists in the hectohertz region of the silicon electrode (green line) is unresponsive to changes in frequency based on surface engineering. In conclusion, the combination of electrode material and substrate surface engineering produces heterogeneity, yet with consistency, in the SPE response.

The complex impedance is often separated into its real and imaginary components,

$$Z^* = \text{Re}(Z) + i \text{Im}(Z) = Z_R + i X_C, \quad (3)$$

where  $Z_R$  is the resistance and  $X_C$  is the reactance. Ohmic resistors exposed to an external AC voltage have an exclusively resistive behavior independent of the frequency, i.e.,  $Z^* = Z_R$ . On the contrary, a sinusoidal voltage applied to a capacitor with capacitance  $C$

yields a reactance of  $X_C = (2\pi\omega C)^{-1}$  and  $Z_R = 0$  [54]. Compared to the pristine substrates, the frequency shift observed in the brush-covered substrates can be attributed to the change in the imaginary part of SPE's complex impedance in response to the applied sinusoidal voltage in EIS. An increase in frequency directly affects the reactance  $X_C$ , reducing the capacitive behavior while enhancing charge mobility.

Further impedance data were scrutinized by investigating both stability and interaction behavior between the input sinusoidal voltage and the ion-conducting material, consisting of the coordination between ether oxygen atoms from the PEO backbone and lithium ions. The electric modulus,  $M$ , quantifies the dielectric relaxation and stability with respect to the externally applied sinusoidal frequency [53,55–57]. The maximum in the imaginary part of the electric modulus signifies the stability threshold of the PEO–lithium ion complex with respect to changes in the oscillating electric field frequency. The resonance peak marks the frequency threshold between regimes where charge carriers are mobile over long distances and where molecular interactions confine the ions, which can only move within a limited distance [58].  $M$  is defined as the reciprocal of the dielectric permittivity,

$$M^*(\omega) = \Re(M) + i\Im(M) = \frac{1}{\epsilon^*} = i(\omega C_0)Z^*, \quad (4)$$

where  $M^*$  is the complex electric modulus,  $\epsilon^*$  is the complex permittivity,  $\omega$  is the frequency,  $C_0$  is the geometrical capacitance, and  $Z^*$  is the complex impedance. The imaginary part of the electric modulus is given by [59,60]

$$\Im(M(\omega)) = M'' = \omega C_0 \Re(Z). \quad (5)$$

The electric moduli for stainless steel and silicon wafer substrates with and without brushes were studied in terms of the electrical relaxation process, shown in Figure 6a. The stainless steel substrate shows a single resonance peak, shifted to a higher frequency by about two orders of magnitude when covered by a brush, indicated by the black arrow.

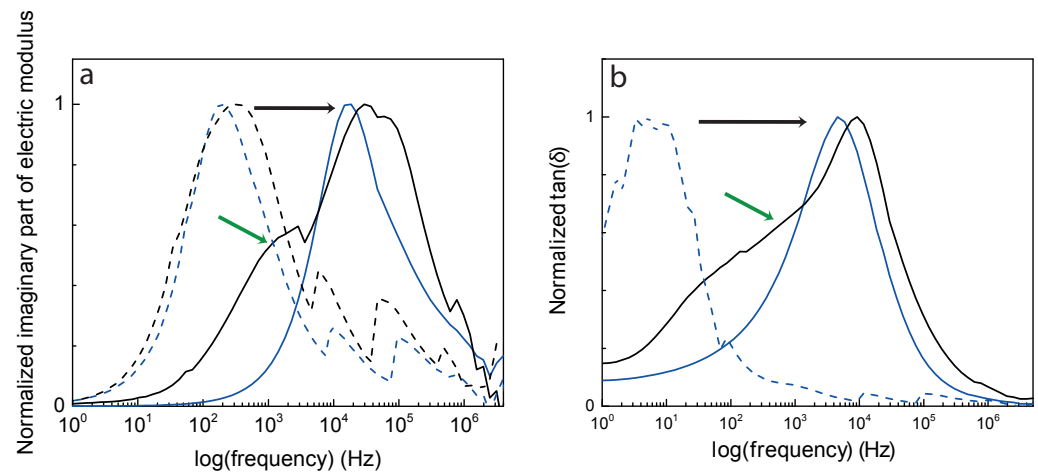


**Figure 6.** Normalized imaginary component of the electric modulus (a) and  $\tan(\delta)$  (b) of PS-*b*-PEO BCP electrolyte sandwiched between pristine (blue dotted line), brush (blue line) stainless steel electrodes, and between pristine (black dotted line), brush-coated silicon wafers (black line). The black arrow highlights the high-frequency shift upon brush functionalization of the substrate, and the green arrow indicates the presence of a new process occurring for the brush-covered silicon substrates.

The increase in the frequency of the relaxation mechanism is accompanied by a stability gain of the dielectric relaxation frequency between lithium ions and PEO chains in relation to the externally applied potential. A low peak frequency of the electric modulus corresponds to a high capacitance caused by charge carrier generation at the electrode/electrolyte interface, resulting in electrode polarization. As frequency increases, the charge carriers dif-

fuse quicker inside the polymeric material, resulting in a decrease in the relaxation time [61]. Because of selective interactions between one of the two copolymer blocks and the pristine substrate, a continuous glassy PS phase forms close to the surface (layer colored in red in Figure 3), interfering with the diffusion of lithium ions through percolation pathways from the interface into the bulk. Covering the surface with a neutral brush reduces the difference in the energetic affinity of the two copolymer blocks, thereby preventing the formation of PS blocking layers against Li-ion diffusion near the substrate. Consequently, long-range ion movement is hampered on the SEO electrolyte when in contact with both pristine substrate types, whereas brush-covered substrate exposes ion conduction channels to the substrate, permitting long-range ion motion from surface to bulk.

The comparison of steel and silicon substrates in Figure 6a reveals the overlap of low- and high-frequency resonances for the pristine and brush-covered substrates, respectively, with higher peak values for the silicon substrates. Moreover, the green arrow indicates a second resonance peak in the mid-frequency range for the brush-covered silicon substrates. Likewise, the pristine silicon substrate expresses the secondary mid-frequency resonance peak, although it is convoluted with the low-frequency peak.

Consistent with the Bode graphs in Figure 5, this additional resonance at mid-range frequencies is seen only for the brush-covered silicon wafer. The silicon substrate mid-frequency peak can be assigned to Li-ion motion in the bulk. Its lower frequency compared to the high-frequency peaks of the brush-covered surfaces probably stems from the lamellar BCP morphology being organized in micrometer-sized domains (“grains”), limiting the long-range motion of ions across grain boundaries.

Moreover, to ensure that the double-peak nature observed for the silicon substrate does not arise from the semicrystalline nature of PEO, Figure S3 shows the electric moduli at 95 °C, a temperature considerably above the melting temperature of PEO, confirming the persistence of the two-peak behavior. Therefore, the nature of the mid-frequency peak arises from a second relaxation mechanism of the polymer-salt dielectric that is only observable when using silicon electrodes. Moreover, the increase in this resonance maximum with temperature suggests that the relaxation is thermally initiated and, therefore, dominated by charge carrier hopping [62].

Finally, similarly to mechanical oscillating systems, the relative energy dissipation of EIS can be considered, quantified by the ratio of the imaginary to the real part of the electric modulus,

$$\tan(\delta) = \frac{\text{Im}(M)}{\text{Re}(M)} = \frac{M''}{M'} = \frac{\text{Re}(Z)}{\text{Im}(Z)} = \frac{Z'}{Z''} \quad (6)$$

$\tan(\delta)$  quantifies the material’s ability to dissipate energy, governed by intrinsic physical processes such as dielectric relaxation, resonance, and losses. In particular,  $\tan(\delta)$  reflects the interaction of the complex formed between the lithium ions and the PEO phase of the BCP with the input sinusoidal potential wave. In terms of the equivalent circuits in Figures 2 and 4, the ratio between loss and storage moduli is associated with the resistive versus capacitive behaviors of the polymeric material, respectively.

The interpolation of the SPE’s decreased capacitive and resistive properties caused by substrate engineering allows for decreased storage and loss moduli. As a result, the shift of  $\tan(\delta)$  to higher frequencies is supported by a reduction in energy dissipation from the SEO BCP, where the system is predominantly resistive over a broader frequency range. The charges in the SPE are also less likely to be stored, enhancing ion mobility.

Because the formation of BCP surface morphologies that differ from the bulk (surface reconstruction) often evolves during thermal annealing, the dependence of the BCP ionic conductivity following a heat treatment was investigated.

Figure 7a shows variations in ionic conductivity with measurement temperature for the BCP SPE sandwiched between silicon wafer substrates. The open and closed symbols correspond to the two Nyquist time constants, and the color coding refers to different annealing temperatures of the sandwiched BCP before the measurements. The range of

annealing temperatures is limited by the thermal stability of the bond that links the brush with the substrate (Table S2).

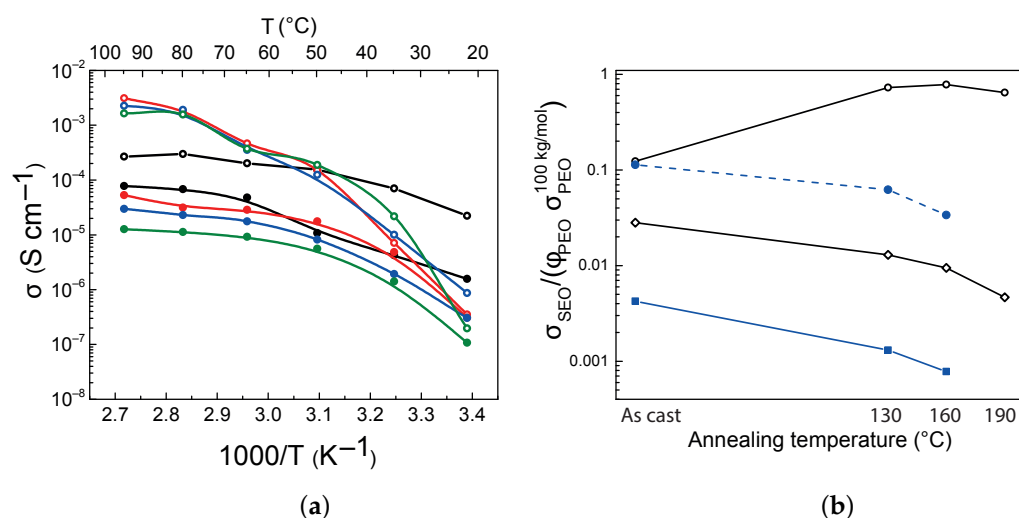


**Figure 7.** (a) Evolution of the PS-*b*-PEO solid polymer electrolyte conductivity sandwiched between two brush-covered silicon wafers before and after thermal annealing. The two different time constants are marked with empty and full symbols. The black, red, blue, and green lines correspond, respectively, to as-cast and annealed at 130 °C, 160 °C, and 190 °C. (b) Two ionic conductivity time constant processes (open black symbols) for the BCP SPE sandwiched between two brush-covered Si wafers, measured at 80 °C, normalized by the PEO volume fraction in the BCP and the values measured for a PEO homopolymer with comparable molecular weight, 100 kg/mol, doped with LiTFSI salt (Figure S7) [63], plotted as a function of thermal annealing temperature. Solid and dashed blue lines correspond to the single time constants of the same SEO copolymer sandwiched between pristine and brush-coated stainless steel electrodes, respectively.

As discussed above, we attribute the higher conductivity values to the BCP behavior close to the electrode surfaces, while the lower conductivities are assigned to the BCP bulk, which, after annealing, differ from each other. Only the conductivity of the SPE very close to the electrode is affected by modifying its surface, i.e., by brush coverage, while the bulk SPE is insensitive to surface chemistries. The conductivity of the former increases upon annealing, indicative of the removal of BCP blocking layers, which hinder ion motion near the surface (Figure 3). The bulk conductivity reduction upon annealing probably arises from the formation and increase in BCP grain boundaries. This behavior is obscured when using stainless steel electrodes, where the single relaxation process of the brush-covered electrode interpolates between the two described processes, and the trend of annealing temperature is dominated by BCP effects (Figure 7b).

The decrease in bulk ionic conductivity attributed to the antagonistic correlation between grain boundaries and ionic conductivity is well established in the literature [39,64]. The enhanced chain mobility above the glass and melting temperatures of the two polymer components enable the release of stresses stemming from the BCP casting procedure, which can cause the formation of additional grain boundaries in the BCP. This alters the percolation pathway for ions to diffuse across inter-grain regions, where the anisotropically oriented grain boundaries may form interfacial layers that hinder ion transport

#### 4. Conclusions

This article uses electrochemical impedance spectroscopy to investigate the ionic conductivity of a LiTFSI-doped PS-*b*-PEO solid electrolyte sandwiched between different electrodes. The ionic conductivities of the BCP SPE sandwiched between stainless steel electrodes reveal a conductivity increase of one order of magnitude when covering the pristine surface with a random P(S-*r*-2VP) copolymer brush. The effect of electrode surface

chemistry on the EIS signal was elucidated by switching from steel substrate to silicon wafer electrodes. A second distinct relaxation process was discerned on silicon electrodes, manifesting as an additional semicircle in the Nyquist plots. Only one of the associated relaxation times was susceptible to the coverage of the silicon electrode with a polymer brush, allowing the surface effects to be disentangled from the ion conductivities in the bulk.

The inability to discern the two time constants using the ubiquitous steel electrodes is probably due to their roughness. Since the described blocking layers likely have length scales of 10s of nanometers, substantial surface roughness would obscure clean measurements of blocking layer effects on the impedance behavior (Figure 3c,d). Silicon wafers, in contrast, feature sub-nanometer roughnesses and are, hence, ideal for the presented analysis. Note, however, that the conclusions obtained also apply to rough surfaces.

The well-established surface reconstruction of BCP in contact with surfaces explains the strong effect of surface ion conductivities. The strong affinity of one of the BCP blocks for the electrode surface causes stratification of the BCP morphology and, hence, blocking layers for ion diffusion. “Neutral” electrode surfaces generated by the surface coverage with a specific random copolymer brush prevent BCP surface reconstruction and open diffusion pathways of the ions to the surfaces.

Examining the electric modulus and the dissipation factor,  $\tan(\delta)$ , reveals tuning of the frequency response; this correlates with a reduction in energy dissipation and decrease in the capacitive behavior of the SPEs, when using brush-covered electrodes, both of which are also indicative of faster ionic motion.

The annealing of the SPE sandwiched between the different electrodes showed interesting trends. Although the ionic conductivities of BCP SPEs typically decrease after annealing with increasing temperatures, the surface conductivity of the brush-covered Si electrodes increased, eventually reaching the theoretical maximum conductivity of the corresponding homopolymer. The former is well established, stemming from BCP grain formation upon preparation-induced stress release. The latter indicates the formation of channels for efficient ion diffusion toward the electrode surfaces as preparation-induced BCP surface blocking layers are annealed away.

For the optimization of BCP SPEs, simultaneous optimization of surface and bulk ionic transport is essential. This study shows how modification of the electrode surfaces enhances ion access to the electrodes, which is critical for device performance. Note that the variation in bulk BCP SPE conductivities upon annealing is a function of annealing time, which was not investigated in this study. The described initial decrease in bulk conductivity is followed by an increase upon coarsening of the BCP grain as grain boundaries annihilate upon sufficient annealing.

While the proposed BCP surface reconstruction at the electrode surfaces is challenging to elucidate by X-ray scattering experiments, future cross-sectional scanning electron microscopy images can provide direct proof for the hypothesis employed in the impedance analyses of this study.

In conclusion, to apply these findings to batteries and supercapacitors that rely on Li-ion migration through the polymer brush, further investigation into the barrier behavior of the P(S-*r*-2VP) copolymer for Li-ion diffusion is required. Although the barrier effects of the 1–2 nm thick layer are likely small, replacing the random copolymer with one containing ethylene-oxide moieties would be preferable to ensure lithium ion diffusion across this layer. Additionally, despite the brush chemical composition, reorienting the BCP domains to enhance conductivity, and consequently, diffusion and transference number at the interface, could help prevent uneven lithium deposition and gradient formation. These two factors contribute to dendritic growth during cell cycling, so addressing them is essential for improving the performance of SPE-based batteries and supercapacitors [65–68].

**Supplementary Materials:** The following supporting information can be downloaded at: <https://www.mdpi.com/article/10.3390/batteries10110401/s1>, Figure S1: complex impedance vs. frequency for the SEO BCP cast onto stainless steel and a silicon wafer; Figure S2: AFM phase images of drop cast BCP with 8% LiTFSI; Figure S3: imaginary component of the electric modulus vs. frequency of the

BCP, measured at 95 °C; Figure S4: Nyquist plot of a pristine silicon wafer measured between two steel electrodes; Figure S5: AFM image of the surface of a polished stainless steel disk; Figure S6: Nyquist plot of the reference PEO homopolymer and the respective Bode plot; Figure S7: ionic conductivity vs. temperature plot of the reference PEO homopolymer; Table S1: water contact angles of stainless steel and silicon substrates; Table S2: thermal stability of the chemical bonding of the random copolymer to the substrate exposed to three organic solvents; Table S3: Nyquist fit parameters of the BCP sandwiched between pristine and brush-covered stainless steel electrodes; Table S4: Nyquist fit parameters of the BCP sandwiched between pristine and brush-covered silicon wafer electrodes.

**Author Contributions:** Conceptualization, I.G.; Methodology, M.A. and I.G.; Validation, U.S.; Formal analysis, M.A.; Investigation, M.A.; Resources, U.S.; Writing—original draft, M.A.; Writing—review & editing, M.A., U.S. and I.G.; Supervision, U.S. and I.G.; Project administration, U.S.; Funding acquisition, U.S. All authors have read and agreed to the published version of the manuscript.

**Funding:** This research was funded by the Adolphe Merkle Foundation.

**Data Availability Statement:** The original contributions presented in the study are included in the article/Supplementary Materials, further inquiries can be directed to the corresponding author.

**Conflicts of Interest:** The authors declare no conflicts of interest.

## References

1. Sashmitha, K.; Rani, M.U. A comprehensive review of polymer electrolyte for lithium-ion battery. *Polym. Bull.* **2023**, *80*, 89–135. [[CrossRef](#)]
2. Wakihara, M. Recent developments in lithium ion batteries. *Mater. Sci. Eng. R Rep.* **2001**, *33*, 109–134. [[CrossRef](#)]
3. Ding, Y.; Cano, Z.P.; Yu, A.; Lu, J.; Chen, Z. Automotive Li-Ion Batteries: Current Status and Future Perspectives. *Electrochem. Energy Rev.* **2019**, *2*, 1–28. [[CrossRef](#)]
4. Choi, C.; Ashby, D.S.; Butts, D.M.; DeBlock, R.H.; Wei, Q.; Lau, J.; Dunn, B. Achieving high energy density and high power density with pseudocapacitive materials. *Nat. Rev. Mater.* **2020**, *5*, 5–19. [[CrossRef](#)]
5. Lewis, G.N.; Keyes, F.G. The potential of the lithium electrode. *J. Am. Chem. Soc.* **1913**, *35*, 340–344. [[CrossRef](#)]
6. Li, B.; Wang, Y.; Yang, S. A Material Perspective of Rechargeable Metallic Lithium Anodes. *Adv. Energy Mater.* **2018**, *8*, 1–16. [[CrossRef](#)]
7. Julien, C.M.; Mauger, A. Review of 5-V electrodes for Li-ion batteries: Status and trends. *Ionics* **2013**, *19*, 951–988. [[CrossRef](#)]
8. Fergus, J.W. Recent developments in cathode materials for lithium ion batteries. *J. Power Sources* **2010**, *195*, 939–954. [[CrossRef](#)]
9. Daniel, C.; Mohanty, D.; Li, J.; Wood, D.L. Cathode materials review. *AIP Conf. Proc.* **2014**, *1597*, 26–43. [[CrossRef](#)]
10. Goriparti, S.; Miele, E.; De Angelis, F.; Di Fabrizio, E.; Proietti Zaccaria, R.; Capiglia, C. Review on recent progress of nanostructured anode materials for Li-ion batteries. *J. Power Sources* **2014**, *257*, 421–443. [[CrossRef](#)]
11. Zhang, H.; Yang, Y.; Xu, H.; Wang, L.; Lu, X.; He, X. Li<sub>4</sub>Ti<sub>5</sub>O<sub>12</sub> spinel anode: Fundamentals and advances in rechargeable batteries. *InfoMat* **2022**, *4*, 1–29. [[CrossRef](#)]
12. Little, A.D.; Park, A. Rechargeable lithium battery anodes: Alternatives to metallic lithium. *J. Appl. Electrochem.* **1993**, *23*, 1–10.
13. Xu, W.; Wang, J.; Ding, F.; Chen, X.; Nasybulin, E.; Zhang, Y.; Zhang, J.G. Lithium metal anodes for rechargeable batteries. *Energy Environ. Sci.* **2014**, *7*, 513–537. [[CrossRef](#)]
14. Liu, Y.K.; Zhao, C.Z.; Du, J.; Zhang, X.Q.; Chen, A.B.; Zhang, Q. Research Progresses of Liquid Electrolytes in Lithium-Ion Batteries. *Small* **2023**, *19*, 2205315. [[CrossRef](#)]
15. Zhang, X.; Wang, A.; Liu, X.; Luo, J. Dendrites in Lithium Metal Anodes: Suppression, Regulation, and Elimination. *Accounts Chem. Res.* **2019**, *52*, 3223–3232. [[CrossRef](#)]
16. Jana, A.; Woo, S.I.; Vikrant, K.S.; García, R.E. Electrochemomechanics of lithium dendrite growth. *Energy Environ. Sci.* **2019**, *12*, 3595–3607. [[CrossRef](#)]
17. Jana, A.; García, R.E. Lithium dendrite growth mechanisms in liquid electrolytes. *Nano Energy* **2017**, *41*, 552–565. [[CrossRef](#)]
18. Takenaka, N.; Bouibes, A.; Yamada, Y.; Nagaoka, M.; Yamada, A. Frontiers in Theoretical Analysis of Solid Electrolyte Interphase Formation Mechanism. *Adv. Mater.* **2021**, *33*, 2100574. [[CrossRef](#)]
19. Horstmann, B.; Single, F.; Latz, A. Review on multi-scale models of solid-electrolyte interphase formation. *Curr. Opin. Electrochem.* **2019**, *13*, 61–69. [[CrossRef](#)]
20. Cheng, X.B.; Zhang, R.; Zhao, C.Z.; Wei, F.; Zhang, J.G.; Zhang, Q. A review of solid electrolyte interphases on lithium metal anode. *Adv. Sci.* **2015**, *3*, 1500213. [[CrossRef](#)]
21. Feng, X.; Ouyang, M.; Liu, X.; Lu, L.; Xia, Y.; He, X. Thermal runaway mechanism of lithium ion battery for electric vehicles: A review. *Energy Storage Mater.* **2018**, *10*, 246–267. [[CrossRef](#)]
22. Wang, Q.; Ping, P.; Zhao, X.; Chu, G.; Sun, J.; Chen, C. Thermal runaway caused fire and explosion of lithium ion battery. *J. Power Sources* **2012**, *208*, 210–224. [[CrossRef](#)]

23. Manthiram, A.; Yu, X.; Wang, S. Lithium battery chemistries enabled by solid-state electrolytes. *Nat. Rev. Mater.* **2017**, *2*, 16103. [[CrossRef](#)]
24. Zhao, Q.; Stalin, S.; Zhao, C.Z.; Archer, L.A. Designing solid-state electrolytes for safe, energy-dense batteries. *Nat. Rev. Mater.* **2020**, *5*, 229–252. [[CrossRef](#)]
25. Zhang, H.; Armand, M. History of Solid Polymer Electrolyte-Based Solid-State Lithium Metal Batteries: A Personal Account. *Isr. J. Chem.* **2021**, *61*, 94–100. [[CrossRef](#)]
26. Devaux, D.; Bouchet, R.; Glé, D.; Denoyel, R. Mechanism of ion transport in PEO/LiTFSI complexes: Effect of temperature, molecular weight and end groups. *Solid State Ionics* **2012**, *227*, 119–127. [[CrossRef](#)]
27. Jiang, Y.; Yan, X.; Ma, Z.; Mei, P.; Xiao, W.; You, Q.; Zhang, Y. Development of the PEO based solid polymer electrolytes for all-solid state lithium ion batteries. *Polymers* **2018**, *10*, 1237. [[CrossRef](#)]
28. Mindemark, J.; Lacey, M.J.; Bowden, T.; Brandell, D. Beyond PEO—Alternative host materials for Li<sup>+</sup>-conducting solid polymer electrolytes. *Prog. Polym. Sci.* **2018**, *81*, 114–143. [[CrossRef](#)]
29. Lee, J.; Kim, B.S. Recent progress in poly(ethylene oxide)-based solid-state electrolytes for lithium-ion batteries. *Bull. Korean Chem. Soc.* **2023**, *44*, 831–840. [[CrossRef](#)]
30. Bates, F.S.; Fredrickson, G.H. Block Copolymers Designer Soft Materials. *Phys. Today* **1999**, *52*, 32–38. [[CrossRef](#)]
31. Glynos, E.; Pantazidis, C.; Sakellariou, G. Designing All-Polymer Nanostructured Solid Electrolytes: Advances and Prospects. *ACS Omega* **2020**, *5*, 2531–2540. [[CrossRef](#)]
32. Cho, B.K.; Jain, A.; Gruner, S.M.; Wiesner, U. Mesophase structure-mechanical and ionic transport correlations in extended amphiphilic dendrons. *Science* **2004**, *305*, 1598–1601. [[CrossRef](#)] [[PubMed](#)]
33. Sax, J.; Ottino, J.M. Modeling of transport of small molecules in polymer blends: Application of effective medium theory. *Polym. Eng. Sci.* **1983**, *23*, 165–176. [[CrossRef](#)]
34. Hallinan, D.T.; Balsara, N.P. Polymer electrolytes. *Annu. Rev. Mater. Res.* **2013**, *43*, 503–525. [[CrossRef](#)]
35. Sethuraman, V.; Pryamitsyn, V.; Ganesan, V. Influence of molecular weight and degree of segregation on local segmental dynamics of ordered block copolymers. *J. Polym. Sci. Part B Polym. Phys.* **2016**, *54*, 859–864. [[CrossRef](#)]
36. Bouchet, R.; Phan, T.N.T.; Beaudoin, E.; Devaux, D.; Davidson, P.; Bertin, D.; Denoyel, R. Charge Transport in Nanostructured PS-PEO-PS Triblock Copolymer Electrolytes. *Macromolecules* **2014**, *47*, 2659–2665. [[CrossRef](#)]
37. Sharon, D.; Bennington, P.; Dolejsi, M.; Webb, M.A.; Dong, B.X.; De Pablo, J.J.; Nealey, P.F.; Patel, S.N. Intrinsic Ion Transport Properties of Block Copolymer Electrolytes. *ACS Nano* **2020**, *14*, 8902–8914. [[CrossRef](#)] [[PubMed](#)]
38. Kambe, Y.; Arges, C.G.; Czaplewski, D.A.; Dolejsi, M.; Krishnan, S.; Stoykovich, M.P.; De Pablo, J.J.; Nealey, P.F. Role of Defects in Ion Transport in Block Copolymer Electrolytes. *Nano Lett.* **2019**, *19*, 4684–4691. [[CrossRef](#)]
39. Chintapalli, M.; Chen, X.C.; Thelen, J.L.; Teran, A.A.; Wang, X.; Garetz, B.A.; Balsara, N.P. Effect of grain size on the ionic conductivity of a block copolymer electrolyte. *Macromolecules* **2014**, *47*, 5424–5431. [[CrossRef](#)]
40. Panday, A.; Mullin, S.; Gomez, E.D.; Wanakule, N.; Chen, V.L.; Hexemer, A.; Pople, J.; Balsara, N.P. Effect of molecular weight and salt concentration on conductivity of block copolymer electrolytes. *Macromolecules* **2009**, *42*, 4632–4637. [[CrossRef](#)]
41. Galluzzo, M.D.; Grundy, L.S.; Takacs, C.J.; Cao, C.; Steinrück, H.G.; Fu, S.; Rivas Valadez, M.A.; Toney, M.F.; Balsara, N.P. Orientation-Dependent Distortion of Lamellae in a Block Copolymer Electrolyte under DC Polarization. *Macromolecules* **2021**, *54*, 7808–7821. [[CrossRef](#)]
42. Shen, K.H.; Brown, J.R.; Hall, L.M. Diffusion in Lamellae, Cylinders, and Double Gyroid Block Copolymer Nanostructures. *ACS Macro Lett.* **2018**, *7*, 1092–1098. [[CrossRef](#)] [[PubMed](#)]
43. Sethuraman, V.; Mogurampelly, S.; Ganesan, V. Multiscale Simulations of Lamellar PS-PEO Block Copolymers Doped with LiPF<sub>6</sub> Ions. *Macromolecules* **2017**, *50*, 4542–4554. [[CrossRef](#)]
44. Sutton, P.; Bennington, P.; Patel, S.N.; Stefik, M.; Wiesner, U.B.; Nealey, P.F.; Steiner, U.; Gunkel, I. Surface Reconstruction Limited Conductivity in Block-Copolymer Li Battery Electrolytes. *Adv. Funct. Mater.* **2019**, *29*, 1905977. [[CrossRef](#)]
45. Coote, J.P.; Kinsey, T.; Street, D.P.; Kilbey, S.M.I.; Sangoro, J.R.; Stein, G.E. Surface-Induced Ordering Depresses Through-Film Ionic Conductivity in Lamellar Block Copolymer Electrolytes. *ACS Macro Lett.* **2020**, *9*, 565–570. [[CrossRef](#)]
46. Coote, J.P.; Adotey, S.K.J.; Sangoro, J.R.; Stein, G.E. Interfacial Effects in Conductivity Measurements of Block Copolymer Electrolytes. *ACS Polym. Au* **2023**, *3*, 331–343. [[CrossRef](#)]
47. Chintapalli, M.; Le, T.N.; Venkatesan, N.R.; Mackay, N.G.; Rojas, A.A.; Thelen, J.L.; Chen, X.C.; Devaux, D.; Balsara, N.P. Structure and Ionic Conductivity of Polystyrene-block-poly(ethylene oxide) Electrolytes in the High Salt Concentration Limit. *Macromolecules* **2016**, *49*, 1770–1780. [[CrossRef](#)]
48. Choudhury, S.; Stalin, S.; Vu, D.; Warren, A.; Deng, Y.; Biswal, P.; Archer, L.A. Solid-state polymer electrolytes for high-performance lithium metal batteries. *Nat. Commun.* **2019**, *10*, 4398. [[CrossRef](#)]
49. Lee, M.J.; Han, J.; Lee, K.; Lee, Y.J.; Kim, B.G.; Jung, K.N.; Kim, B.J.; Lee, S.W. Elastomeric electrolytes for high-energy solid-state lithium batteries. *Nature* **2022**, *601*, 217–222. [[CrossRef](#)]
50. Li, Z.; Yu, R.; Weng, S.; Zhang, Q.; Wang, X.; Guo, X. Tailoring polymer electrolyte ionic conductivity for production of low-temperature operating quasi-all-solid-state lithium metal batteries. *Nat. Commun.* **2023**, *14*, 482. [[CrossRef](#)]
51. Gunkel, I. Directing Block Copolymer Self-Assembly on Patterned Substrates. *Small* **2018**, *14*, 1802872. [[CrossRef](#)] [[PubMed](#)]
52. Mansky, P.; Liu, Y.; Huang, E.; Russell, T.P.; Hawker, C. Controlling polymer-surface interactions with random copolymer brushes. *Science* **1997**, *275*, 1458–1460. [[CrossRef](#)]

53. Tian, F.; Ohki, Y. Electric modulus powerful tool for analyzing dielectric behavior. *IEEE Trans. Dielectr. Electr. Insul.* **2014**, *21*, 929–931. [[CrossRef](#)]
54. Lazanas, A.C.; Prodromidis, M.I. Electrochemical Impedance Spectroscopy—A Tutorial. *ACS Meas. Sci. Au* **2023**, *3*, 162–193. [[CrossRef](#)] [[PubMed](#)]
55. Hodge, I.; Ngai, K.; Moynihan, C. Comments on the electric modulus function. *J. Non-Cryst. Solids* **2005**, *351*, 104–115. [[CrossRef](#)]
56. Coşkun, M.; Polat, A.O.; Coşkun, F.M.; Durmuş, Z.; Caglar, C.M.; Türüt, A. The electrical modulus and other dielectric properties by the impedance spectroscopy of LaCrO<sub>3</sub> and LaCr<sub>0.90</sub>Ir<sub>0.10</sub>O<sub>3</sub> perovskites. *RSC Adv.* **2018**, *8*, 4634–4648. [[CrossRef](#)]
57. Chérif, S.F.; Chérif, A.; Dridi, W.; Zid, M.F. AC conductivity, electric modulus analysis, dielectric behavior and Bond Valence Sum analysis of Na<sub>3</sub>Nb<sub>4</sub>As<sub>3</sub>O<sub>19</sub> compound. *Arab. J. Chem.* **2020**, *13*, 5627–5638. [[CrossRef](#)]
58. Liu, J.; Duan, C.G.; Yin, W.G.; Mei, W.N.; Smith, R.W.; Hardy, J.R. Large dielectric constant and Maxwell-Wagner relaxation in Bi<sub>2/3</sub>Cu<sub>3</sub>Ti<sub>4</sub>O<sub>12</sub>. *Phys. Rev. B* **2004**, *70*, 144106. [[CrossRef](#)]
59. Ram, M.L.; Chakrabarti, S. Dielectric and modulus studies on LiFe<sub>1/2</sub>Co<sub>1/2</sub>VO<sub>4</sub>. *J. Alloy. Compd.* **2008**, *462*, 214–219. [[CrossRef](#)]
60. Saif, A.A.; Poopalan, P. AC Conductivity and Dielectric Relaxation Behavior of Sol-gel Ba<sub>x</sub>Sr<sub>1-x</sub>TiO<sub>3</sub> Thin Films. *J. Mater. Sci. Technol.* **2011**, *27*, 802–808. [[CrossRef](#)]
61. Verma, M.L.; Sahu, H.D. Ionic conductivity and dielectric behavior of PEO-based silver ion conducting nanocomposite polymer electrolytes. *Ionics* **2015**, *21*, 3223–3231. [[CrossRef](#)]
62. Wan, T.H.; Saccoccio, M.; Chen, C.; Ciucci, F. Influence of the Discretization Methods on the Distribution of Relaxation Times Deconvolution: Implementing Radial Basis Functions with DRTtools. *Electrochim. Acta* **2015**, *184*, 483–499. [[CrossRef](#)]
63. Irwin, M.T.; Hickey, R.J.; Xie, S.; So, S.; Bates, F.S.; Lodge, T.P. Structure–Conductivity Relationships in Ordered and Disordered Salt-Doped Diblock Copolymer/Homopolymer Blends. *Macromolecules* **2016**, *49*, 6928–6939. [[CrossRef](#)]
64. Sedlak, P.; Gajdos, A.; Macku, R.; Majzner, J.; Holcman, V.; Sedlakova, V.; Kubersky, P. The effect of thermal treatment on AC/DC conductivity and current fluctuations of PVDF/NMP/[EMIM][TFSI] solid polymer electrolyte. *Sci. Rep.* **2020**, *10*, 21140. [[CrossRef](#)]
65. Kerr, J.B.; Han, Y.B.; Liu, G.; Reeder, C.; Xie, J.; Sun, X. Interfacial behavior of polymer electrolytes. *Electrochim. Acta* **2004**, *50*, 235–242. [[CrossRef](#)]
66. Zhao, Y.; Wang, L.; Zhou, Y.; Liang, Z.; Tavajohi, N.; Li, B.; Li, T. Solid Polymer Electrolytes with High Conductivity and Transference Number of Li Ions for Li-Based Rechargeable Batteries. *Adv. Sci.* **2021**, *8*, 2003675. [[CrossRef](#)] [[PubMed](#)]
67. Wang, Y.; Fu, L.; Shi, L.; Wang, Z.; Zhu, J.; Zhao, Y.; Yuan, S. Gel Polymer Electrolyte with High Li<sup>+</sup> Transference Number Enhancing the Cycling Stability of Lithium Anodes. *ACS Appl. Mater. Interfaces* **2019**, *11*, 5168–5175. [[CrossRef](#)]
68. Cui, M.; Fu, S.; Yuan, S.; Jin, B.; Liu, H.; Li, Y.; Gao, N.; Jiang, Q. Dual Interface Compatibility Enabled via Composite Solid Electrolyte with High Transference Number for Long-Life All-Solid-State Lithium Metal Batteries. *Small* **2024**, *20*, 2307505. [[CrossRef](#)]

**Disclaimer/Publisher’s Note:** The statements, opinions and data contained in all publications are solely those of the individual author(s) and contributor(s) and not of MDPI and/or the editor(s). MDPI and/or the editor(s) disclaim responsibility for any injury to people or property resulting from any ideas, methods, instructions or products referred to in the content.